Simulation of pressure-driven phase transitions from tetrahedral crystal structures

Mark Wilson
Department of Chemistry, University College London, 20 Gordon Street, London WC1H 0AJ, United Kingdom

Francis Hutchinson* and Paul A. Madden
Physical and Theoretical Chemistry Laboratory, Oxford University, South Parks Road, Oxford OX1 3QZ, United Kingdom
(Received 24 August 2001; published 12 February 2002)

Pressure-driven transitions of ionic materials from the zinc-blende to rocksalt and δ-$ZnCl_2$ to $CdCl_2$ crystal structures are studied using constant-stress molecular dynamics with a polarizable-ion potential model. Both transformations are characterized by a change in cation coordination environment from tetrahedral to octahedral and are nonmartensitic. Transformation mechanisms are identified and characterized and similarities discussed. The blende to rocksalt transformation is observed to proceed via a diatomic β-tin-like structure, though this is shown to be a transition state and not a true intermediate phase in this system. The relationship of the observed mechanisms to those deduced from experiments on halide systems is discussed. The development of displacive motion across the simulation cell is discussed. The $ZnCl_2$ system is a layered structure, and while the coordination changes are highly cooperative within each layer, the overall transformation takes place on a layer-by-layer basis. In the blende, the interlayer correlations required to produce a grain-boundary-free final structure are associated with a shearing motion which propagates across the cell. These differences have characteristic effects on the kinetics of the transformations.

DOI: 10.1103/PhysRevB.65.094109 PACS number(s): 61.50.Ks, 62.50.+p, 02.70.Ns

I. INTRODUCTION

Numerous II-VI and III-V semiconductors crystallize in the four-coordinate zinc-blende or wurtzite crystal structures and exhibit phase transitions to six-coordinate structures, particularly rocksalt, at high pressure. The same transitions also notably occur in the copper and silver halides. Nelmes McMahon[1] have conducted an extensive crystallographic study of these transitions, particularly in the semiconducting materials, identifying numerous intermediate phases and potential transition pathways. In some cases the relative stability of these intermediates has been examined using *ab initio* methods,[2–6] so that a comprehensive, though complex, picture is beginning to emerge. In addition, Sowa has recently considered possible mechanistic pathways for the blende $\rightarrow$rocksalt[7] and the wurtzite$\rightarrow$rocksalt transition,[8] purely in terms of the crystal symmetries (following an analogous analysis of the rocksalt to CsCl transition.[9]) High-pressure studies of the halides have been carried out, particularly by Hull and co-workers,[10–17] who identify other intermediate phases in these relatively ionic materials. That the mechanism of the transition is likely to be complex and material specific can be appreciated from the realization that in both the blende and rocksalt structures the anion sublattices are cubic close packed with the cations in (one-half of) the tetrahedral holes in blende and the octahedral holes in rocksalt. Thus the transition involves a shift of one sublattice with respect to the other; it clearly cannot be achieved by a simple deformation of the unit cell (like the martensitic rocksalt to CsCl transition). How the ions avoid a high-energy intermediate state as they move past each other will clearly depend on the details of their interaction.

Further interest in these transitions has been introduced by the demonstration, by Tolbert and Alivisatos,[18] that the pressure of the transition for nanoparticles suspended in an inert medium is *very* strongly affected by the particle size (as also is the rate and hysteresis of the transition). This effect can be traced to the effect of the particle surface on the thermodynamics of the transition.[19] Since different mechanisms will expose different crystalline faces in the course of the transition, the extent of the particle size dependence could depend strongly on which mechanism is adopted and the habit of the initial microcrystallite. It is even possible that a different mechanism could be adopted in the nanoparticle than the bulk or that semiconductor nanoparticles could be prepared in a metastable high-pressure phase if the transition pathway is blocked by an unfavorable surface energy contribution. In a subsequent paper we will contrast the blende mechanism with that observed for the wurtzite to rocksalt transition for the same ionic potential. The mechanisms turn out to be qualitatively different, and we will show that this is a consequence of the different stacking sequences in the blende and wurtzite structures.

Using constant-stress molecular dynamics simulations, in which an isotropic pressure is progressively increased, we have examined the mechanism of the blende to rocksalt transition for a model ionic interaction potential (called ''MCl,'' crudely representing, at least in ionic size ratio, LiCl or CuCl). Sowa's[7] consideration of the mechanism from a general symmetry-based perspective leads to the idea that the pathway adopted between the two phases should not be greatly influenced by the detailed form of the interaction potential. However, this will affect such material-specific details as whether particular points upon the pathway are associated with metastable intermediate phases. By using the molecular dynamics (MD) method we allow the system to find its own transition pathway at finite temperature, as opposed to examining the relative energies of the system along some particular postulated pathway (as is more common in the computationally demanding electronic structure calcula-

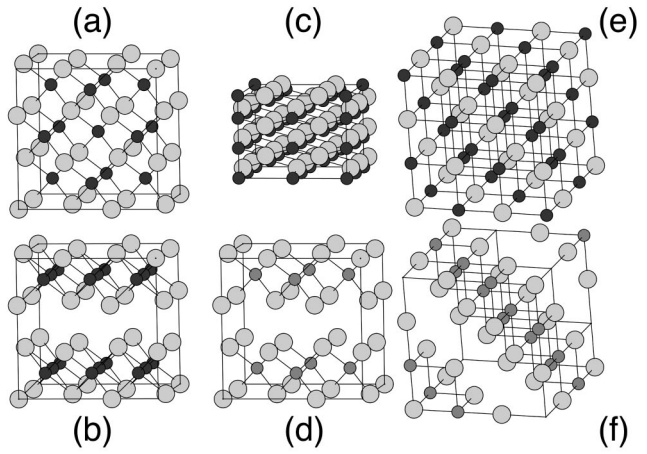

FIG. 1. Crystal structures for four MX systems and two MX_2. Key: large circles, anions; small, dark circles, M^+ cations; lighter, small circles, M^{2+} cations. (a) Blende, $B3$, (b) antilitharge, (c) diatomic-β-tin, (d) δ-$ZnCl_2$, (e) rocksalt, $B1$, and (f) $CdCl_2$.

tions). The difficulty comes in identifying the pathway which has been chosen by observation of the ionic trajectories.

We have also studied the δ-$ZnCl_2$ to $CdCl_2$ transition (for a model of $ZnCl_2$) which, despite the different stoichiometry, is closely related to the blende ($B3$) to rocksalt ($B1$) transition. The δ-$ZnCl_2$ and $CdCl_2$ are also based upon the occupation of tetrahedral and octahedral holes in a cubically close-packed anion sublattice. As shown in Fig. 1 the relationship between the pairs of structures $B3/\delta-ZnCl_2$ and $B1/CdCl_2$ is that in each case the latter structure is obtained by removing alternate planes of cations from the former, resulting in a ''sandwich'' structure. This means that the cation displacements involved in the δ-$ZnCl_2 \rightarrow CdCl_2$ phase transition are similar to those in $B3 \rightarrow B1$ but decoupled to a greater degree.

We use polarizable-ion model (PIM) potentials, in which the instantaneous-induced dipoles on the ions are dynamical variables in the simulation procedure. We first describe the potentials and characterize their low-energy crystal structures from energy-volume curves. Polarization effects are particularly important for the $ZnCl_2$ system, where the phase transition is between two layered crystal structures which[20,21] are stabilized by anion polarization effects. Using these potentials allows us to study quite large simulation cells and to ramp the pressure relatively slowly, compared to *ab initio* simulations.[22] This is important because the movement of a cation out of its tetrahedral site is linked to a large deformation of the unit cell which contains it, and this generates a large strain on neighboring cells whose effect can only be properly represented if the simulation contains a large number of unit cells.

For the constant-stress simulations we need an expression for the stress tensor for the PIM potentials, and we outline how this is obtained. We then study the dynamics of the phase transition for the $ZnCl_2$ system which shows a concerted rearrangement of the ions within each layer, but no correlation between layers, and then the MCl blende transition. Finally, we discuss the effect of various parameters controlling the simulation (such as the system size and the rate at which the pressure is ramped) upon the observations.

II. SYSTEMS UNDER STUDY: OVERVIEW

A. Blende→rocksalt

A large number of systems of MX stoichiometry undergo a transition from the cubic blende ($B3$) to the rocksalt ($B1$) structure on application of moderate pressure. The $B3$ and $B1$ structures are simply related, both consisting of a face-centred-cubic array of anions in which half of the tetrahedral holes ($B3$) or all of the octahedral holes ($B1$) are filled, respectively. These structures are shown in Fig. 1 along with four related structures which will be discussed below.

The most common class of compounds undergoing such a transition are the II-VI and III-V semiconductors.[1] In addition, CuCl, CuBr, and CuI all show such a transition[14–17] along with AgI.[10–13] For both semiconductors and halides a range of intermediates has been observed (see, for example, Refs. 1,2,14–17, and 23). The β-tin structure is observed as a high-pressure phase of both Si and Ge (Ref. 1) generated from the ambient diamond phase (ZnS is isostructural to diamond, but is a diatomic crystal). The contraction of the lattice along one direction brings a pair of next-nearest neighbors about a given atom into close range, effectively increasing the atom coordination from 4 to 4+2. The site-ordered diatomic equivalent (d-β-Sn, also illustrated in Fig. 1) has long been proposed as an intermediate for a range of semiconductor pressure-driven phase transitions.[1] Recent work, however, has cast doubt on the existence of such a phase.[1,24] For AgI, for example, powder neutron diffraction studies suggest a tetragonal intermediate in the antilitharge structure in which the I^- ions form an essentially cubic close-packed structure with the Ag^+ cations occupying half of the available tetrahedral holes but in planes rather than in the tetrahedral occupancy pattern of the blende structure as can be seen from Fig. 1.[10] Keen and Hull[10] propose a plausible mechanism for the $B3 \rightarrow B1$ transition via such an antilitharge structure involving the rearrangement of the cation sublattice with minimal changes in the anion lattice. Moore and Kasper[25] suggest an alternative, although still tetragonal, intermediate.

"MCl" potential

We have studied the blende→rocksalt transition with a potential obtained in an attempt to describe LiCl by scaling a successful potential for NaCl to allow for the change in cation size. NaCl had been modeled with an effective pair potential of the Born-Mayer form

$$u_{BM}^{ij}(r^{ij}) = B^{ij} e^{-a^{ij} r^{ij}} + \frac{Q^i Q^j}{r^{ij}} - \frac{C_6^{ij}}{r^{ij6}}, \qquad (2.1)$$

augmented with a full description of the anion dipole polarization using a polarizable-ion model as discussed previously (see, for example, Ref. 21). In Eq. (2.1) the first term represents the short-range repulsion between the ions, the second is the charge-charge interaction, and the third is the dipole-dipole dispersion interaction. The dipole polarization effects

TABLE I. Born-Mayer potential parameters for MCl (Ref. 47) and $ZnCl_2$ (Ref. 42). All are in atomic units.

Ion pair	MCl			$ZnCl_2$		
	a^{ij}	B^{ij}	C_6^{ij}	a^{ij}	B^{ij}	C_6^{ij}
$--$	1.55	61.66	116.0	1.0	8.0	200.0
$-+$	1.55	8.678	2.09	1.6	48.0	0.0
$++$	1.55	1.146	0.08	1.56	19.6	40.0

are described by assigning a dipole moment to each anion and determining its value (the ''adiabatic dipole'') at each time step by minimizing the interaction energy which contains charge-dipole, dipole-dipole, and a Drude-like self-energy. In this respect, the PIM contains the same physics as a shell model, except that the short-range polarization is not simply assumed to be proportional to the short-range force; it takes a form uncovered in direct *ab initio* studies of the polarization in distorted crystals.[26–28] It is convenient to update the adiabatic dipoles by borrowing ideas from the Car-Parrinello method of *ab initio* MD. The dipolar PIM requires two input parameters to specify the polarization: the anion polarizability and the short-range damping parameter (SRDP). Both can be calculated *ab initio* in the condensed environment (see, for example, Refs. 26–30). For the MCl model, the anion polarizability is taken as 20.0 a.u. with the cation taken as unpolarizable. The damping parameter is 1.75 a.u. with a preexponent of $c=2.0$.[27,28]

The potential terms most affected by such a change in cation size are the short-range repulsion between cation and anion, for which the amplitude B^{MCl} [Eq. (2.1)] scales (crudely) as

$$B^{LiCl}=e^{a^{NaCl}(\sigma^{Li^+}-\sigma^{Na^+})}B^{NaCl}, \tag{2.2}$$

and the short-range damping parameter b^{MCl}, which scales[21] as

$$b^{LiCl}=b^{NaCl}\frac{\sigma^{Na^+}+\sigma^{Cl^-}}{\sigma^{Li^+}+\sigma^{Cl^-}}, \tag{2.3}$$

where σ is the ionic radius. The scaled potential parameters are given in Table I.

Calculated energy versus volume curves for various optimized crystal structures obtained with this potential are given in Fig. 2. They show that the lowest-energy crystal structure for this potential is wurtzite ($B4$), with the blende structure only slightly higher in energy ($\sim$2.0 kJmol^{-1}). The wurtzite and blende structures are both obtained by occupying with cations the tetrahedral holes in a close-packed anion lattice, except that in the former the anions are hexagonally close packed whereas in the blende they are cubic, so that this similarity in energies is to be expected. At a lower molar volume and higher energy we find that the rock-salt ($B1$) structure and the common tangent construction predicts a $B4\rightarrow B1$ transition at a pressure of 5.7 GPa. The $B2$ (CsCl, eight-coordinate ions) phase is at a significantly less negative energy than either the $B1$ or $B3/4$. As a result,

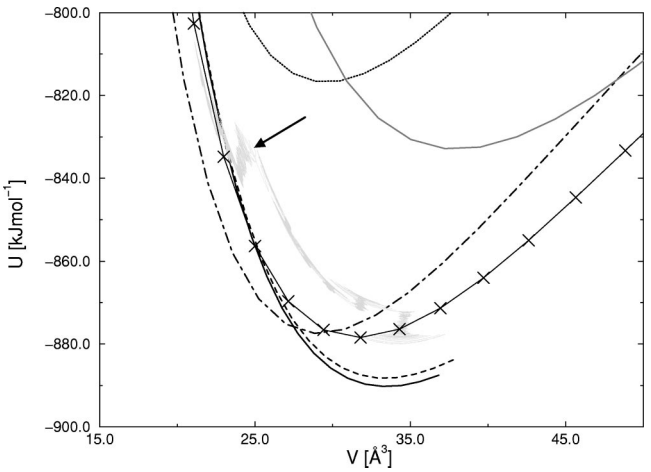

FIG. 2. Energy-volume curves for the MCl potential. Key: solid line, $B4$ (lowest energy); dashed line, $B3$; dot-dashed line, $B1$; solid line, $\times$, d-β-Sn with $c/a=0.64$; light solid line, antilitharge; dotted line, $B2$. The light line is the dynamic energy-volume evolution during the phase transition. The arrow indicates the point at which the $B3$ structure starts to change.

this phase can be discounted from our present considerations. The other curves shown (for the d-β-Sn and antilitharge structures) will be used in the discussion of the transition mechanisms below.

However, these predictions for the scaled potential are at odds with the experimental situation for LiCl, which crystallizes in the $B1$ phase. This failure is associated with with the representation of the short-range repulsion in the Born-Mayer potential because, in the perfect $B1$, $B3$, and $B4$ crystal structures, the site symmetry is too high for any ionic polarization. It can be understood by reference to previous calculations on alkaline-earth oxides[31,32] and CsCl.[33] In those cases it was shown how pair potentials systematically favor structures of lower coordination number, as the effect of the change in size of the anion with coordination number is not represented. As a result, a single pair potential derived for a given coordination number does not transfer well to an alternative environment. For oxides, this effect is large as the O^{2-} ion is only stabilized by the crystal field and, as a result, is very sensitive to its environment. For halides the effect is relatively small. However, in cases such as CsCl, and here LiCl, where the energy difference between two possible polymorphs is small, such effects become important.

For our immediate purpose, to study mechanisms for tetrahedral to octahedral transitions, the failure to obtain a good potential for LiCl is fortuitous, as it means we have an easy-to-use potential (the ''MCl'' potential) which will exhibit such transitions at moderate applied pressure. To obtain a faithful representation for LiCl, we should develop a ''compressible-ion'' potential, as in the work on oxides.[31,34]

B. δ-$ZnCl_2\rightarrow CdCl_2$

Under moderate (<5 GPa) pressures $ZnCl_2$ transforms from a four-coordinate (δ-$ZnCl_2$) structure to a six-coordinate ($CdCl_2$) crystal[35] as monitored experimentally by

Raman spectroscopy[36] and x-ray diffraction[37] studies. Both crystal structures are based on a packed layered motif in which infinite anion-cation-anion ''sandwiches'' stack on top of one another. An alternative viewpoint is to consider the anion sublattice as pseudo-close-packed. For the δ-$ZnCl_2$ structure one-quarter of the tetrahedral holes are filled by cations, while the $CdCl_2$ structure has half of the octahedral holes filled. The relationship between the four-coordinate structures δ-$ZnCl_2$ and blende and the six-coordinate $CdCl_2$ and rocksalt can be seen by considering Fig. 1. To transform the blende into the δ-$ZnCl_2$, half of the cations occupying the tetrahedral holes are removed in layers perpendicular to a $<100>$ direction. To transform from the rocksalt to the $CdCl_2$, however, the cations in the octahedral sites are removed in successive layers perpendicular to a $<111>$ direction. In both cases, the pattern of occupancy leads to the planes of holes between close-packed anion layers being alternately filled and unfilled, leading to the sandwich structure. However, the layers in the two structures are not in the same orientation with respect to the underlying close-packed anion sublattice. The $(MX_2)_\infty$ layers in both structures are charge neutral and so the layer-layer interactions are dominated by weak van der Waals (dispersion) forces. Hartree-Fock *ab initio* calculations, which contain no dispersion, show how structures of this type are unstable with respect to separation of the layers.[38]

$ZnCl_2$ may be unique in having such a layered→layered structural transformation. A more common pressure-driven transition pattern for systems of this stoichiometry is from the relatively open (low density) four-coordinate silicalike structures to a more close-packed six-coordinate rutile structure. Such transitions are observed experimentally in, for example, BeF_2, SiO_2, and GeO_2.[39,40]

Potential for $ZnCl_2$

Simple pair potentials (''rigid-ion models''[20,21]) fail to predict the stability of these classes of crystal structure since the nearest-neighbor cation-cation separations are equivalent to the anion-anion distance despite the fact that the cations carry double the formal charge. However, the anions in the layered structure sit in highly asymmetric environments having a complete layer of cations on one side (whether they be in tetrahedral or octahedral holes) but a totally empty layer on the other side. This asymmetry leads to a large resultant electric field acting on the anion site inducing large dipole moments whose negative ends point down into the cation layers. The negative ends of the dipoles effectively screen the relatively large cation-cation repulsion. The polarization energy in these systems accounts for around a quarter of the total lattice energy.[20]

The parameters for the $ZnCl_2$ model (see Table I) are taken from earlier work[41,42] in which it was shown to reproduce a number of important properties such as the Raman spectra.[41,42] The anion polarizability is again taken as 20.0 a.u. with the cations assumed unpolarizable. The damping parameter is 1.55 a.u. with a preexponent of $c=1.0$.[27] The predicted ground-state crystal structure is the δ-$ZnCl_2$ and (from the common tangent to the static internal energy versus cell volume curves for the optimized crystal structures) it is predicted to make a transition to the denser, six-coordinate ($CdCl_2$) crystal at an applied pressure of 0.6 GPa.

III. SIMULATION DETAILS

A. Constant-stress molecular dynamics

The constant pressure method of Andersen[43] was extended by Parrinello and Rahman[44] to allow the simulation box to change shape as well as size. Later it was realized that the equations of motion are not invariant to the initial choice of cell frame, and several invariant schemes were proposed. We have implemented the equations of motion as given by Martyna *et al.*[45] In the most flexible model the cell can undergo full relaxation in that both the cell lengths and angles may vary, but it is also possible to allow purely tetragonal or isotropic cell fluctuations within the same scheme. The ions and the barostats are both coupled to Nosé-Hoover chains of length 5. We experienced no problems in coupling these extended equations of motion to the equations of motion controlling the induced dipoles in the PIM scheme. All long-range interactions (up to terms which vary with interionic separation as r^{-4}) are described by the Ewald method, adapted to noncubic cells as described by Nosé and Klein.[46] We impose a fixed spherical cutoff at r_c on the interactions in real space and terminate the run if the cell becomes so anisotropic that this cutoff becomes larger than the smallest repeat distance of the periodic boundary conditions. We choose an Ewald convergence parameter η such that $\eta r_c = 5.6$ (Ref. 47) and vary the number of k vectors in the reciprocal-space sum as the cell shape varies to ensure a given degree of convergence.

In order to complete these equations, we need an expression for the stress tensor. This is nonstandard, since the ''additional'' variables (dipoles, etc.) of the polarizable-ion model play a role, in addition to the pairwise additive forces which have been considered previously (e.g., by Nosé and Klein[46]). The total stress tensor is given by

$$\Pi_{\alpha\beta}^{tot}=\frac{1}{V}\sum_i M_i \dot{r}_{i,\alpha}\dot{r}_{i,\beta}+\Pi_{\alpha\beta}, \tag{3.1}$$

where the the configurational part of the stress tensor $\Pi_{\alpha\beta}$ is to be obtained from[46]

$$-\frac{\partial U}{\partial h_{\alpha\beta}}=\sum_\gamma \Pi_{\alpha\gamma} V h_{\beta\gamma}^{-1}. \tag{3.2}$$

Here U is the total potential energy, V the cell volume, and $\mathbf{h}$ is the cell matrix, whose elements are the components of vectors along the simulation cell edges. The derivatives with respect to the elements of $\mathbf{h}$ thus give the rate of change of the interaction energy as the shape and size of the simulation cell is varied due to the changes in the interionic separations which this brings about. The particular difficulty is that the interaction energy depends upon the dipoles on the ions as well as the ionic positions, i.e.,[34]

$$U\equiv U(\{\mathbf{r}^i\}_{i=1,N},\{\boldsymbol{\mu}^i\}_{i=1,N}), \tag{3.3}$$

and the change in dipoles with respect to a change in cell shape would appear to contribute to the derivative. However, the forces on the ions are to be determined with the dipoles taking their ''adiabatic'' values, $\{\overline{\mu^i}\}_{i=1,N}$, i.e., those which minimize U for each ionic configuration. We may therefore exploit the Hellmann-Feynman theorem,[48] analogous to that used to calculate the forces on the ions from a variationally optimized *ab initio* electronic structure calculation, to write

$$\frac{\partial U}{\partial h_{\alpha\beta}} = \sum_j \frac{\partial U}{\partial \mathbf{r}^j}(\{\mathbf{r}^i\}_{i=1,N}, \{\overline{\mu^i}\}_{i=1,N}) \cdot \frac{\partial \mathbf{r}^j}{\partial h_{\alpha\beta}}, \qquad (3.4)$$

and ignore the derivative of the dipoles with respect to the change in cell shape.

In the Ewald construction the interaction energy is decomposed into real-space and reciprocal-space components

$$U(\{\mathbf{r}^i\}_{i=1,N}, \{\mu^i\}_{i=1,N}) = U^{real}(\{\mathbf{r}^i\}_{i=1,N}, \{\mu^i\}_{i=1,N}) + U^{recip}(\{\mathbf{r}^i\}_{i=1,N}, \{\mu^i\}_{i=1,N}), \qquad (3.5)$$

where U^{real}, in the PIM, is a sum of pairwise additive terms, which converge at a range shorter than the simulation cell length, plus a Drude-like self-energy, which depends only on the dipoles and not the ionic positions. Consequently, the real-space contributions to the stress tensor can be expressed in the standard virial form (i.e., $\sim \Sigma_{ij,pairs} r_\alpha^{ij} f_\beta^{ij}$, where $\mathbf{f}^{ij}$ is the real-space contribution to the force between i and j). The reciprocal-space contribution was derived by developing the Appendix of Nosé and Klein's paper,[46] which gives the reciprocal-space energy expression for a system of molecules with internal charges, to charged, dipolar species. Expressions for the charge-charge, charge-dipole, and dipole-dipole contributions to the stress tensor are given in the Appendix.

B. Inducing and monitoring the transition

In order to study pressure-driven phase transitions, we need to be able to increase (or decrease) the pressure in a well-controlled fashion. Our aim must be to move relatively slowly through the pressure range over which any transition may occur rather than to shock the system via a sudden application of more pressure than required. To this end we have investigated two basic schemes which were found to give identical pressure transitions under the same simulation conditions. In the first scheme, the external pressure is ''ramped'' at predetermined points in the simulation by a predetermined pressure increment Δp. In the present work, Δp was typically taken as 10^{-4}a.u. ($\equiv 3$ GPa) ramping every 10 000 time steps ($\simeq 6$ ps). This time period was found to be significantly longer than that required for the internal pressure to equilibrate about the new value. In the alternative scheme the pressure was ramped continuously over the whole run with a ramp of Δp around 10^{-9}a.u. applied at each time step. Since both procedures were found to locate identical pressure transition points, then the first scheme will be applied throughout as it is more flexible in terms of locating unknown transition pressures, the second scheme being only really applicable when the pressure transition point has been predetermined.

For $ZnCl_2$, simulations were performed using 128 molecules starting from an ideal δ-$ZnCl_2$ crystal (corresponding to $4\times4\times2$ unit cells) with the layers set up to be parallel to the xy plane. The system temperature is held at 100 K, changing the pressure by 2×10^{-5} a.u. ($\simeq 0.6$ GPa) every 10 000 time steps with barostat parameters τ_b of 50 000 a.u. This is related to the barostat masses (W and W_{g0}) discussed by Martyna and co-workers[45] by

$$W = (N_f + d) kT \tau_b^2,$$

$$W_{g0} = (N_f + d) kT \tau_b^2 / d, \qquad (3.6)$$

where N_f is the number of degrees of freedom ($3N-3$ for N particles) and d is the system dimensionality (3). A (very) small time step of 5 a.u. was used throughout in order to allow for relatively smooth dynamics through the phase transition. The temperature was controlled throughout using a Nosé-Hoover thermostat with a relaxation time of 10 000 a.u.

For MCl the simulations are performed on systems containing between 216 and 1000 ions at 300 K, using a time step of 25 a.u. ($\simeq 0.6$ fs). Nosé-Hoover thermostats and barostats are employed throughout with a NH-thermostat relaxation time of 50 000 a.u. and barostat parameters of 10 000 a.u.

C. "Powder" structure factors

Although the simulations give direct access to the atomic trajectories and, therefore, a level of detail inaccessible to the experimentalist, because of thermal and other sources of disorder, it may be difficult to recognize which crystal structure best describes the overall arrangement of the atoms in the simulation cell. We have found it useful to calculate the effective powder diffraction pattern from the simulation cell and to compare this with the diffraction patterns which would be obtained from idealized crystal structures. The partial structure factors are calculated directly at every molecular dynamics time step,

$$S_{\alpha\beta}(k) = A_\alpha(k) A_\beta^*(k). \qquad (3.7)$$

Here, $A_\alpha(k)$ is the scattering amplitude of species α given by

$$A_\alpha(k) = \sum_{i=1}^{N_\alpha} e^{i\mathbf{k}\cdot\mathbf{r}_i}, \qquad (3.8)$$

where the scattering vectors $\mathbf{k}$ are the reciprocal lattice vectors of the periodically replicated simulation system at the time step of interest. The ''powder'' pattern is obtained by averaging over scattering vectors of equal length. For these crystalline systems the structure factors consist of a series of well-defined Bragg peaks. The total structure factor is then constructed from the three partial functions

$$F(k) = b_M^2 c_M [S_{MM}(k) - 1] + 2 b_X b_M \sqrt{c_X c_M} S_{MX}(k) + b_X^2 c_X [S_{XX}(k) - 1], \tag{3.9}$$

where b_α is the scattering length and c_α the mole fraction of species α. Since we are interested only in assigning the structures to known crystal structures, we shall set $b_M = b_X$, that is, assume both ions to scatter equally.

D. Elastic constants

In addition to the dynamical simulations, static crystal calculations are also performed on the ideal $B3$ crystals over the range of volumes encountered during the application of the dynamic pressure in order to calculate the three surviving elastic constants C_{11}, C_{12}, and C_{44}. In such a cubic crystal the stability criteria can be expressed in terms of the three elastic stiffness tensors[2,49–51]

$$\frac{1}{3}(B_{11} + 2B_{12}) > 0,$$

$$B_{44} > 0,$$

$$\frac{1}{2}(B_{11} - B_{12}) > 0, \tag{3.10}$$

where these are related to the simple elastic constants via

$$B_{11} = C_{11} - p,$$

$$B_{12} = C_{12} + p,$$

$$B_{44} = C_{44} - p. \tag{3.11}$$

The first stability criterion (the spinodal criterion) is equivalent to a finite-pressure bulk modulus. The second term (the shear criterion) is the stability to a shear along the [111] direction, while the third (Born) criterion is equivalent to a finite-pressure shear modulus.

C_{11} and C_{12} are calculated from the bulk modulus $[B = (1/V) d^2U/dV^2 \equiv \frac{1}{3}(C_{11} + 2C_{12})]$ and the shear modulus $[C_s = \frac{1}{2}(C_{11} - C_{12})]$. The bulk modulus is generated simply from the static energy-volume curves. To calculate the shear modulus the strain matrix

$$\boldsymbol{\epsilon} = \begin{pmatrix} \frac{2\delta}{3} & 0 & 0 \\ 0 & \frac{-\delta}{3} & 0 \\ 0 & 0 & \frac{-\delta}{3} \end{pmatrix} \tag{3.12}$$

was applied with δ ranging from -0.006 to $+0.006$ a.u. (well within the harmonic range). To calculate C_{44} the strain matrix

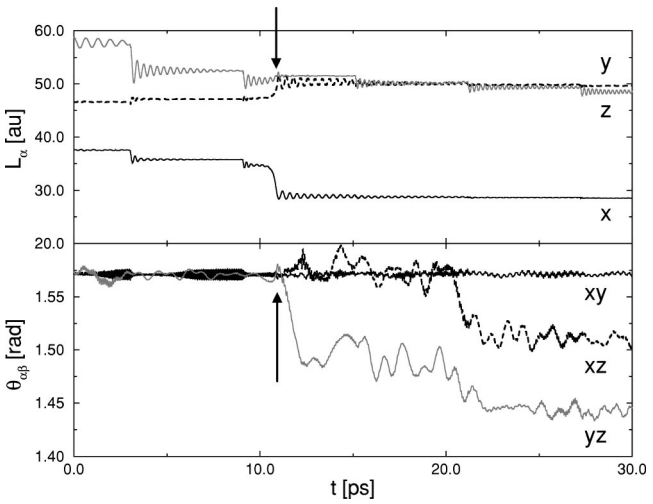

FIG. 3. Time evolution of the cell lengths (upper panel) and angles (lower panel) for the simulation of $ZnCl_2$. The pressure is periodically increased as described in the text. The arrows indicate the time at which there is significant structural transformation.

$$\boldsymbol{\epsilon}_2 = \begin{pmatrix} 0 & \frac{\delta}{2} & \frac{\delta}{2} \\ \frac{\delta}{2} & 0 & \frac{\delta}{2} \\ \frac{\delta}{2} & \frac{\delta}{2} & 0 \end{pmatrix} \tag{3.13}$$

is applied with the same δ values.

IV. δ-$ZnCl_2 \rightarrow CdCl_2$

We begin by discussing the $ZnCl_2$ transition, for which the mechanism is easier to explain than the one we find for MCl, but turns out to be closely related to it.

Figure 3 shows that time evolution of the simulation cell lengths and angles for the $ZnCl_2$ simulation model starting from the orthorhombic $ZnCl_2$ structure.[36] The simulation cell is initially oriented such that the layers lie perpendicular to the [001] direction (along the z axis). The arrows indicate the time at which a significant change in both the cell lengths and angles begins to occur. The changes in lengths and angles appear to occur simultaneously with a compression along the x axis and slight expansions along both the y and z axes accompanied by a shearing motion indicated by the change in angle between the xy and xz planes. The changes in the cell angles after ~ 20 ps are driven by a further increase in the pressure which causes the layer-layer packing to rearrange.

Figure 4 shows the sequence of ionic positions around 10 ps where the transformation occurs. The view is down the y direction of the simulation cell so that, initially, we see layers of cation-centered tetrahedra connected by their vertices. The contraction of the cell along the x direction corresponds to the ''squashing'' of the tetrahedra in this direction. This contraction is accompanied by a highly correlated shift in the cation positions within each cation layer, as shown in the

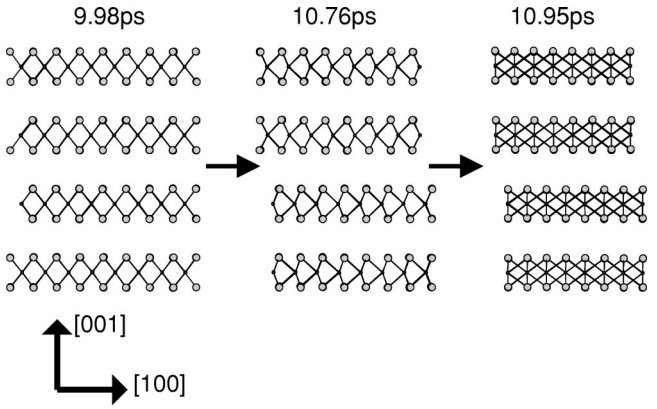

FIG. 4. Molecular graphics snapshots for three time steps around the structural transformation of $ZnCl_2$. The left panel (9.98 ps) shows the layers in the initial δ-$ZnCl_2$ structure with the right-hand panel showing the layers in the final $CdCl_2$ structure. The central panel shows an intermediate configuration in which the cations in each layer are moving in a highly correlated fashion.

second panel of the figure. The layered nature of the crystal means that the cation motions in different layers are relatively weakly correlated, so that, in the example shown, the cations in the upper two layers have shifted to the left, whereas those in the lower two layers have shifted to the right. The cation shift is coupled with a shearing motion (as already evident from the change in simulation cell angles) which results in the formation of a new closed-packing arrangement of the anions. The three panels in the figure are oriented in the same sense. The apparent major change in the anion-anion separations in the third panel compared with the first is a direct result of the change in orientation of the close-packed anion sublattice. As demonstrated by comparison with Fig. 1, the first panel in Fig. 4 has a close-packed anion sublattice in a different orientation to that found after the transformation (the third panel).

The change in layered crystal, with the subsequent change in cation coordination number from 4 to 6, is accompanied by a change in the polarization energy from ~ -160 to ~ -140 kJ mol^{-1}. This change is fully consistent with the increase in the Zn-Cl bond length (from 4.6 to 4.8 a.u.) as the coordination number increases.

Figure 5 shows the pressure-volume curves for the $ZnCl_2$ transition. The volume change going through the transformation is relatively smooth (unlike the $B3 \rightarrow B1$ transition which shows a distinct ''jump'' in volume — see later). The pressure required to transform the crystal (~ 1.6 GPa) is greater than the static transformation pressure calculated from the 0 K energy-volume curves (~ 0.6 GPa). This is an overpressure required to drive the phase transformation over the kinetic barrier which is appropriate to the particular conditions of the simulation (simulation cell size, etc.). The overpressure can be considered in terms of a thermodynamics driving force[52] with

$$\Delta G(p) = \Delta V(p - p_t), \tag{4.1}$$

where p_t is the ideal transition pressure and p the actual pressure at which the transition is observed to occur. By

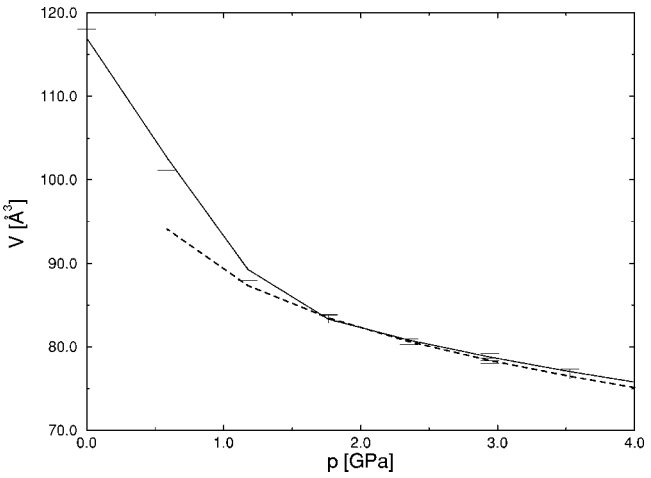

FIG. 5. Pressure-volume curves for the δ-$ZnCl_2 \rightarrow CdCl_2$ phase transformation. The solid line is for the forward transformation and the dashed line for the reverse.

taking ΔV as a constant over the whole pressure range (determined at p_t) we can estimate the free energy barrier. The barrier for the forward (δ-$ZnCl_2 \rightarrow CdCl_2$) transformation is $\simeq 3.5$ kJ mol^{-1}, which turns out to be significantly smaller than for any of the other transformation considered here (see Table II).

V. MCl ZINC-BLENDE → ROCKSALT TRANSFORMATION

Figure 6 shows the time evolution of the cell lengths and angles for the MCl simulation of 1000 molecules ($5 \times 5 \times 5$ cubic unit cells) at 300 K with the pressure increased in steps of 10^{-4}a.u ($\cong 3$ GPa) every 10 000 time steps ($\equiv 6.05$ ps). At $\simeq 40$ ps, with a system pressure around 15 GPa, the three equivalent cell lengths decouple with two lengths increasing (L_y and L_z) with a corresponding reduction in the third length (L_x). At around the same time the cell angles also change with θ_{yz}, moving from 90° to around 110°. These changes are associated with a volume reduction of 11% and increase in bond lengths from 2.03 to 2.25 Å. Figure 6 highlights the short time period over which the transition occurs. The thick dashed lines are drawn to highlight the difference in time between the changes in the cell lengths and angles and show that the changes in cell lengths occur prior to the changes in cell angles. The initial tetragonal distortion of the cell occurs at $\simeq 39.4$ ps with the first change in cell angle at $\simeq 39.7$ ps ($\simeq 500$ time steps later). The change in cell angles is correlated with a further

TABLE II. Phase transformation data for the two studied changes. Key: P_t, static transformation pressure; P_t', pressure range required in the dynamic simulation to drive the phase transition; ΔV, volume change on transformation; ΔG^{over}, energy required to drive the phase transition.

System	P_t (0 K) (GPa)	P_t' ($\Rightarrow$) (GPa)	ΔV (%)	ΔG^{over} (kJ mol^{-1})
LiCl	4.8	15.0–21.0	11.3	19.0
$ZnCl_2$	0.6	1.2	10.1	3.5

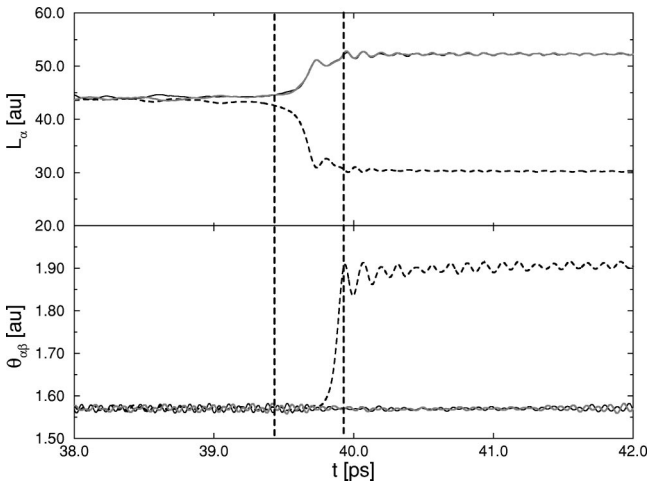

FIG. 6. Time evolution of the cell lengths and angles for the MCl $B3 \rightarrow B1$ phase transformation. The dashed lines highlight the time lag between the changes in the cell lengths and angles.

(smaller) change in the cell lengths. Note that, although these changes are analogous to those observed for $ZnCl_2$ above, the time lag between the two ''stages'' of the transformation is a difference. In the $ZnCl_2$ case they occur simultaneously.

Figure 7(a) shows the time evolution of the total structure factor $F(k)$ as the system is driven through the transition characterized by the changes evident in the previous figures. The structure factors are calculated, as described above, at a series of time steps through the region in which the cell lengths, etc., change dramatically. Figure 7(b) highlights three of these functions [shown as bold in Fig. 7(a)]. They are taken at times (a) initial, before any change in cell lengths is observed; (b) intermediate, in the region where cell lengths have changed but not yet cell angles; and (c) final, after the major change of lengths and angles is complete. These structure factors are compared with the total structure factors corresponding to three idealized structures, along with the Bragg peak assignments. The peak assignments, coupled with the comparison with idealized crystal structure factors, confirm the initial and final structures as being $B3$ and $B1$ respectively (we will discuss the intermediate result below).

Figure 8 shows the p-V curve for the present run (the curve showing the lowest transition pressure in the figure) along with four other such curves for a smaller system using a range of barostat parameters (see Sec. VI for a discussion of the effect of the barostat parameters on the observed behavior). The figure also shows the value of the static transition pressure (4.8 GPa) calculated from the 0 K energy volume curves. It is clear that the overpressure, required to drive the system over the barrier between the two phases, is significantly larger here than for the $ZnCl_2$ transformation (see Table II). Furthermore, Fig. 8 shows a significant ''jump'' in volume at the transition pressure, unlike the $ZnCl_2$ case where there is a more continuous variation in the cell volume.

Figure 9 shows the evolution of both the shear modulus $[C_s \equiv \frac{1}{2}(C_{11}-C_{12})]$ and C_{44} elastic constant, along with the corresponding elastic stiffness tensors, as a function of lattice

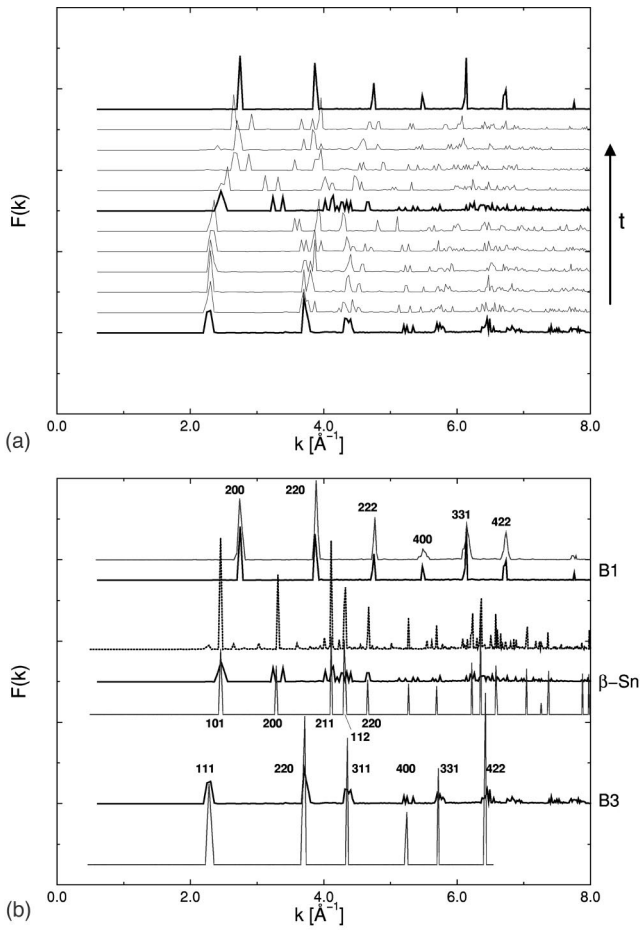

FIG. 7. (a) Time evolution of the total structure factors during the dynamic phase transformation. In (b), the three highlighted functions in (a) are compared to ideal calculated functions. For the central (d-β-Sn) functions, the lowest line is the ideal function while the upper line is the structure factor calculated from a configuration in which the ions have been allowed to relax from the dynamic configuration.

parameter for the $B3$ phase. The Born criterion ($B_s > 0$) is violated at the lattice parameter corresponding to the required static transformation pressure, whereas the shear criterion ($B_{44} > 0$) holds to much lower lattice parameters (higher pressures). The violation of the Born criterion is characteristic of the sort of shear motion of the anion sublattice observed above in which layers of ions slide over each other to form a new close-packed lattice.

A. Mechanism: Local changes in coordination polyhedra

Since it is known that the transformation mechanism is nonmartensitic, we might anticipate a relatively complex mechanism involving a range of length scales and correlation lengths. At the simplest level, however, we may consider the transformation in terms of the nearest (and next-nearest) neighbor interactions. Figure 10(a) shows a schematic representation of the observed structural transition mechanism. The first step is the initial tetragonal distortion, signaled by the changes in cell lengths described above, in which the

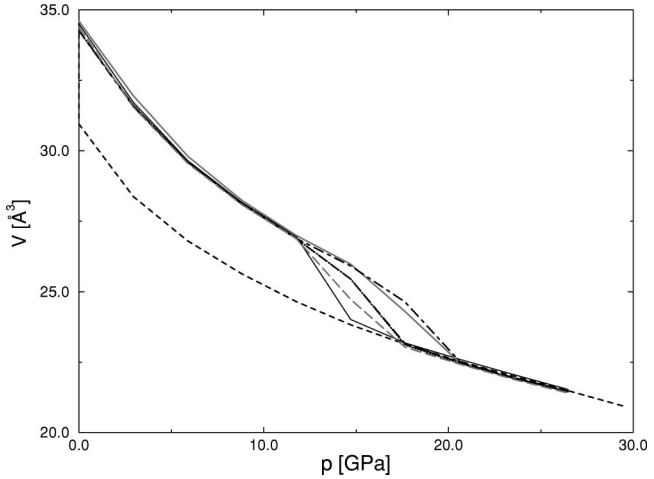

FIG. 8. Pressure-volume curves for the MCl phase transition. Key: 216 ions unless stated. The results for the run described in the main body of the paper are shown by the solid black line and correspond to a barostat parameter, $\tau = 10\,000$ a.u. The effect of changing the barostat parameter, discussed in Sec. VI, is shown by the other curves; light-dashed line, $\tau = 50\,000$ a.u.; dot-dashed line, $\tau = 75\,000$ a.u.; dashed line, $\tau = 100\,000$ a.u.; light line, $\tau = 10\,000$ a.u.; 1000 ions.

anion and cation planes are compressed in the $[100]_{B3}$ direction with a corresponding expansion in the $[010]_{B3}$ and $[001]_{B3}$ directions. This ''transition'' is driven by the increase in cation coordination number from four in the ideal $B3$ structure to an effective 4+4 (as shown in the figure). The c/a ratio is around 0.64 with a nearest-neighbor bond length of 2.06 Å and a next-nearest anion-cation separation of 3.16 Å. The nearest-neighbor length appears to be still very much like that in the $B3$ precursor rather than the $B1$ ''product.''

In the second stage the cation sublattice moves as shown to form a local coordination polyhedron in which each cation is surrounded by two anions and four slightly further away (2+4 coordination) at $\simeq 2.05$ and 2.30 Å, respectively. This

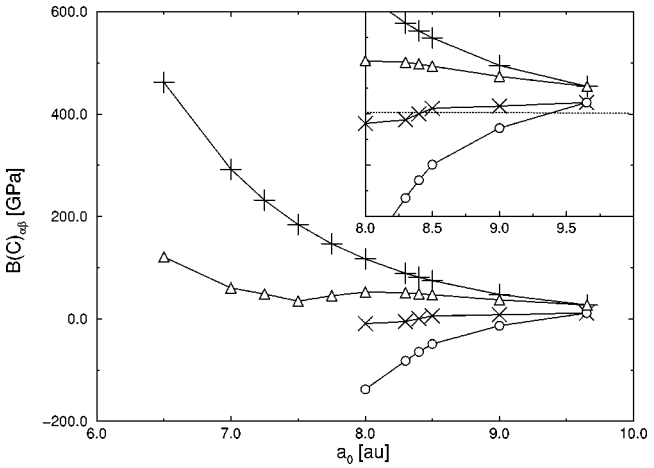

FIG. 9. Variation of the elastic constants for the $B3$ structure with lattice parameter. Key: +, C_{44}; △, B_{44}; ×, C_{11}-C_{12}; ○, B_{11}-B_{12}.

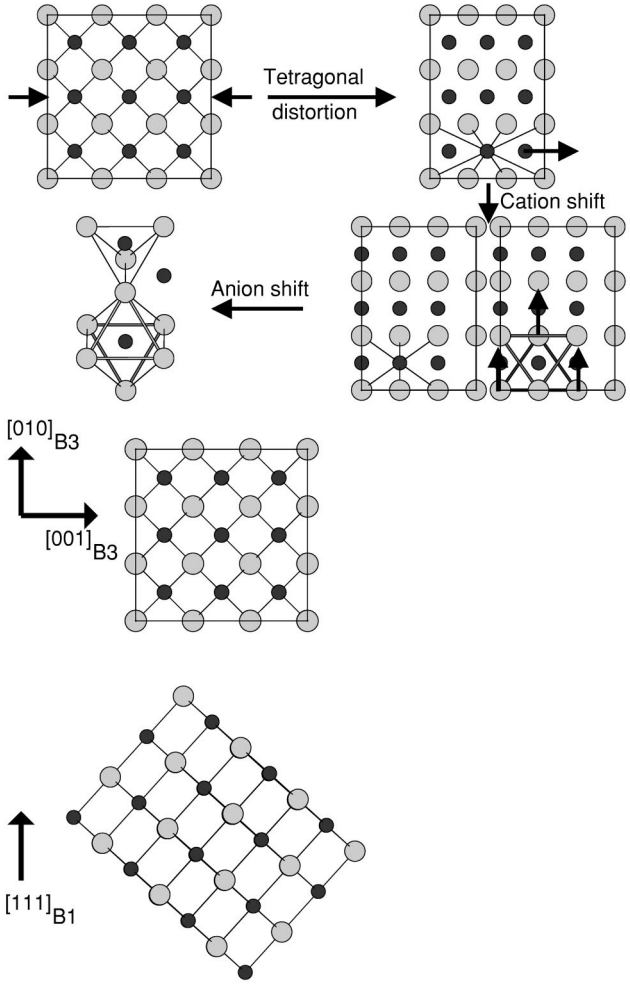

FIG. 10. (a) Schematic representation of the $B3$ to $B1$ model transformation mechanism. The initial transformation is characteristic of a $B3 \rightarrow d$-β-Sn distortion, the second stage is the correlated motion of the cations, and the third stage has the anion sublattice shearing to form a new octahedral hole. Panel (b) highlights the change is close-packed anion lattice during the transformation.

cation motion is accompanied by a concerted shift in the anion sublattice along the $[001]_{B3}$ direction as indicated by the arrows. The result of this second stage is that the triangle of anions (indicated with arrows) in the $[101]_{B3}$ plane, slides over the layer beneath forming the ''star of David'' characteristic of a cation in an octahedral hole viewed along the $[111]_{B1}$ direction.

The six nearest-neighbor anions in the newly formed octahedron consist of the four anions originally in the nearest-neighbor tetrahedron along with two anions gained from the next-nearest neighbors. As a result, therefore, the observed mechanism is displacive in that two bonds have been formed while none have been broken.

The overall result of these changes, which strongly resemble those illustrated above for $ZnCl_2$, is that the cation now sits in a near-perfect octahedral hole in which the original $[010]_{B3}$ direction of the blende structure becomes the

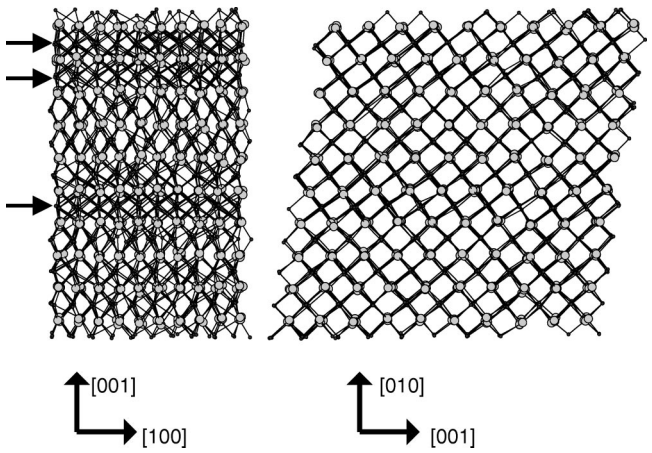

FIG. 11. Molecular graphics snapshots for the 1000-ion $B3 \rightarrow B1$ transformation during the second stage in Fig. 10. The arrows indicate layers in which the cations have shifted to forming octahedral holes.

$[111]_{B1}$ of the rocksalt. To highlight this point further, Fig. 10(b) shows the initial and final crystals viewed in the $[011]_{B3}$ plane. Note that, although both the anion and cation sublattices have remained close packed, they have reoriented during the transformation going through a non-closed-packed ''intermediate.''

B. Structural changes beyond nearest neighbors

While it is possible to understand the basic $B3 \rightarrow B1$ transformation mechanism is terms of the evolution of the local coordination polyhedra, it is clear that the reconstructive nature of the mechanism must lead to significant correlated motion of both the anion and cation sublattices over a range of length scales. The initial tetragonal distortion itself [Fig. 10(a)] occurs uniformly throughout the whole cell. The second stage, in which the cations shift, is more complex; not all cations shift simultaneously.

It is clear from Fig. 10(a) that, in the (ideal) tetragonal cell, the 4+4 coordinate cation is in a highly symmetric site. As a result, the subsequent cation motion to obtain the six-coordination of the $B1$ structure is *a priori* equally likely be be in either the $[100]_{B3}$ or $[\bar{1}00]_{B3}$. However, only if all cations actually move in the same direction will a perfect $B1$ crystal result. How these correlations develop is indicated in Fig. 11, which shows a snapshot of the cell during the intermediate stage of $B3 \rightarrow B1$ transition. As indicated by the arrows in the figures, three layers of cations can be seen to have shifted towards octahedral sites, in the way indicated in Fig. 10(a). The remaining seven layers are still clearly in the 4+4 ''intermediate'' coordination environment. The right-hand side of Fig. 11 shows the same time snapshot from a viewpoint which is perpendicular to the viewpoint adopted in the left-hand side, so that corresponding layers appear at the same vertical height in the two images. The formation of the octahedral sites in the arrowed layers is indicated in the right-hand image by the more rectangular appearance of the $(MX)_2$ planes compared to the near-square units in the 4+4 layers [see also Fig. 10(b)]. The existence of considerable stresses between the transformed and untransformed cells is evident from the bending of the planes of ions along the diagonals of the right-hand figures.

Figure 11 shows how the cation motion is correlated strongly in the $[100]_{B3}$ and the $[010]_{B3}$ directions (so that all the cations in a given xy plane have shifted simultaneously) and relatively weakly along the $[001]_{B3}$ direction (so that only three out of ten of the layers are caught in the act of shifting, and of these only two are adjacent). The fact that the final configuration is an ideal $B1$ crystal indicates that the cation motion must also eventually be correlated in the $[001]_{B3}$ direction. The development of these correlations is related to the shearing of the simulation cell in the second stage of the transition. The anion sublattice shifts as shown in Fig. 10(a) with $\{110\}_{B3}$ layers cascading over each other to form a new close-packed lattice. If the direction of cation motion were reversed between an adjacent pair of layers, a grain boundary would be created in the final crystal configuration (see last section).

C. Relationship between the $B3 \rightarrow B1$ and δ-$ZnCl_2 \rightarrow CdCl_2$ mechanisms

It is clear from the discussion of the observed mechanisms that the model $B3 \rightarrow B1$ and δ-$ZnCl_2 \rightarrow CdCl_2$ transformations are closely related, at least at the local level. This is, in a sense, not surprising since the initial and final structures essentially differ only in the occupancy of the tetrahedral and octahedral holes, respectively. The differences in mechanisms can be attributed to the layered nature of both the starting material and end product in the MX_2 stoichiometry. The alternation of layers of filled and unfilled holes has removed the correlation between cation positions perpendicular to the layers, so that the transition can occur more or less independently in each layer (see Fig. 4). In the $B3 \rightarrow B1$ transition we saw how these correlations were important in determining whether a perfect $B1$ crystal or a series of grain boundaries was formed. These differences are reflected in the difference in the pressure-volume curves (Figs. 5 and 8). The $B3 \rightarrow B1$ curve shows a distinct ''jump'' in volume about the pressure of the phase transition. The δ-$ZnCl_2 \rightarrow CdCl_2$ transformation, however, shows a more gradual change in volume, reflecting the relative ease by which pressure changes can be accommodated by rearranging the packing of the individual layers.

The difference is also reflected in the driving energies listed in Table II. The relative lack of cation-cation interactions between layers means that the driving overpressure required to force this transformation is significantly smaller than for the $B3 \rightarrow B1$.

D. Possible role of intermediate phases

1. β-tin structure

As noted, the $B3 \rightarrow B1$ transformation seems to occur in two stages, accompanied by an initial tetragonal distortion and a subsequent shearing. We might ask whether the configurations of the system in between these two stages (first step in Fig. 10) should be considered as an intermediate

phase, as frequently discerned from time-resolved crystallographic studies. This tetragonal distortion of the $B3$ structure is characteristic of the so-called diatomic β-tin (d-β-Sn) structure.

In order to show how our observed ''intermediate'' corresponds to a $B3 \rightarrow d$-β-Sn distortion, we have compared the structure factor calculated at the intermediate position in the dynamical transition [Fig. 7(b)] with that calculated for an ideal d-β-Sn structure with a c/a ratio of 0.64 [the lowest curve of the three in Fig. 7(b)], corresponding to the ratio observed for our intermediate. The agreement between this ideal function and that calculated dynamically as the system changes phase is very good. Furthermore, we have taken an ionic configuration from the intermediate portion of the MD simulation and performed a steepest-descent minimization of the ion positions while holding the cell lengths fixed and calculated the total structure factor (uppermost curve of the three in the figure). Here, the agreement between this and the ideal function is excellent. A more subtle point relevant here is whether this is actually a tetragonal d-β-Sn structure or a proposed orthorhombic distortion of symmetry I_{mm2}.[1] The splitting of the [200] peak in the dynamic total structure factor indicates that, at this point in time, the a and b unit cell lengths are distinct (the [200] and [020] Bragg peaks are resolved). However, the fact that this splitting disappears when the ion positions are relaxed indicates that this splitting is simply the result of the dynamic fluctuations and that the locally optimised structure is essentially tetragonal.

The c/a ratio observed in the present work (~ 0.64) is significantly larger than those observed experimentally for high pressure Si and Ge ($c/a \sim 0.4$ in the cubic cell, ~ 0.55 in the tetragonal cell). In order to investigate the relationship between the system energy and the c/a ratio, static energy-volume curves were calculated for c/a ratios ranging from 1 (ideal $B3$) down to 0.4 (the experimentally observed ratios for Si and Ge). Figure 2 shows a single such curve calculated for $c/a = 0.64$ (the ratio observed for our intermediate). The curves for ratios lower than this have minima at significantly higher energies. For $c/a = 0.4$, for example, the energy minimum is at around -730 kJ mol^{-1} compared with the $B3$ energy minimum at around -890 kJ mol^{-1}. This behavior can be rationalized in terms of a simple ionic model. In the monatomic diamond$\rightarrow\beta$-Sn phase transition, the contraction of the cell along one axis brings two next-nearest-neighbor atoms into next-nearest-neighbor positions (increasing the coordination number from 4 to 4+2). In fact, for a c/a ratio of $\sqrt{\frac{4}{15}}$ the coordination number would become exactly 6. In the site-ordered d-β-Sn structure, all of the nearest-neighbor ions are of the opposite type to the given central ion, that is, of the opposite charge. This charge ordering is essentially imposed in highly ionic systems because the energetic penalty for having like ions as nearest neighbors is relatively high. In the d-β-Sn structure, however, the next-nearest-neighbor ions to a selected central ion are of the *same* type to that central ion. As a result, as the lattice distorts this repulsive ion-ion interaction acts to try to restore the $B3$ structure. In an ionic model, such as the one imposed here, such interactions are so energetically unfavorable as to limit the accessible range of c/a ratios.

The true role of the d-β-Sn-like intermediate configurations becomes clear from a careful consideration of Fig. 2. At a volume of ~ 25 Å^3/molecule, the d-β-Sn structure with a c/a ratio of 0.64 becomes energetically favorable over the $B3$ and, since the $B3 \rightarrow d$-β-Sn transition is martensitic, the structural transformation proceeds relatively easily. However, at this volume Fig. 2 also indicates that the $B1$ structure is now energetically favorable with respect to *both* the B3 and d-β-Sn. This indicates that the d-β-Sn structure is *not* a true intermediate in this system, but is a metastable state which arises as the martensitic $B3 \rightarrow d$-β-Sn transition proceeds rapidly compared with the reconstructive d-β-Sn $\rightarrow B1$. To support this conclusion further, Fig. 2 also shows the energy-volume curve for the dynamic phase transition simulation at 300 K. It appears to show the instantaneous potential energy hopping from the surface appropriate to one crystal structure to another in the sequence discussed. The arrow indicates the volume at which the $B3$ structure distorts to the d-β-Sn.

It is worth noting that the majority of systems for which this intermediate has been proposed are semiconductors. As a result, there may well be particular features of the electronic structure, not present in simple ionic models, which act to favor the formation of homopolar (like-like) bonds and, as a result, help to stabilize lower c/a ratios.

In order to confirm that the d-β-Sn structure is a transition state rather than a genuine intermediate, we can attempt to isolate the structure by halting the simulation with the cell in the tetragonal geometry (at around 39.5 ps) and relax the ions into their local energy minima while allowing the cell geometry to evolve. Both the ions and the cell are then released and allowed to evolve under their equations of motion while periodically removing the kinetic energies. A true intermediate would remain in the initial cell geometry while a transition structure will simply pass either to the starting and product material. In this case we find that the structure always progresses to the final $B1$ structure and, as such, cannot be considered as a genuine intermediate.

It is important to note that the proposed mechanism is entirely consistent with that proposed by Sowa[7] from group theoretical considerations. By considering the symmetries of both the initial blende and final rocksalt structures he reduced the overall pathway into two steps comprising a displacive ion motion along [100] and a distortion of the whole lattice which appears as a combined shear and tetragonal distortion. In the present work, the lattice undergoes an initial distortion (towards a d-β-Sn structure) *followed* by ion motion in the [100] direction (consistent with the first part of the two-step motion considered by Sowa) to form a new octahedral site, followed by a further shearing distortion.

2. Relationship to the γ-AgI to rocksalt AgI mechanism

It is of interest to see if the mechanism observed in the current work has any relationship to that derived by Keen and Hull for AgI from powder neutron diffraction studies.[10] It might be expected that our MCl system might behave more similarly to the ionic AgI rather than the more covalent

semiconducting systems. In the Keen-Hull mechanism the blende structure transforms into the rocksalt through a tetragonal antilitharge intermediate. In a tetragonally distorted blende unit cell the cation at $(\frac{1}{2},\frac{1}{2},\frac{1}{2})$ moves along the c axis to $(\frac{1}{2},\frac{1}{2},0)$, accompanied by a change in the anion sublattice in which it moves away from being close packed to form the antilitharge structure. The direction of this cation motion is along the $[100]_{B3}$ direction in Fig. 10(a) and so is equivalent to that observed in the present work. Although the direction of this displacement is the same in both mechanisms, the differences lie in both the magnitude of the displacement and the number of ions involved. To form the antilitharge intermediate (see Fig. 1) only half of the cation sublattice must displace from one set of tetrahedral holes to two of the vacant holes (forming the planes of silver cations). In the mechanism described above *all* of the cations shift in this direction but stop when they reach the line joining two nearest-neighbor anions, that is, halfway to the empty tetrahedral site on the other side of these ions. Clearly, if all the ions moved in the AgI mechanism, the blende structure would be reformed but with the cations in the ''alternative'' close-packed tetrahedral hole array. Furthermore, the present mechanism involves a tetragonal distortion of the lattice as a precursor to the shift in the cation sublattice, while the AgI mechanism involves the same type of distortion *during* the shift of cations.

In addition, the γ-AgI$\rightarrow$ rocksalt-AgI mechanism leaves the orientation of the I^- sub-lattice unchanged whereas the present mechanism, although beginning and ending with the anions in a close-packed arrangement, involves a relatively large shift in the anion sublattice such that the orientation of the close-packed array changes across the transition. Such a difference would affect the predicted change of shape of a nanocrystallite undergoing the transition *inter alia*.

We can speculate that the reason for the difference in mechanism observed here and that for AgI. In the latter, the cation sublattice is known to be extremely mobile, with the formation of a superionic phase at low temperature. It is possible, therefore, that the greater cation mobility is indicative of the presence of lower activation energy pathways in which the cation can effectively pass from one tetrahedral site to a neighboring (originally vacant) site. For less mobile cations such motion requires the anion sublattice to undergo a significant rearrangement in order to accommodate the cation on the anion-anion edge.

Figure 2 shows the energy-volume curve calculated for an antilitharge structure. The layered nature of this structure means that, unlike in the ideal $B3$ or $B1$ structures, polarization effects are significant. Indeed, litharge structures formed by both PbO and SnO can be rationalized in terms of cation polarization effects.[53,54]. In the present model, the energy minimum for the antilitharge structure in the absence of polarization effects is at ~ -730 kJ mol^{-1}, ~ 160 kJ mol^{-1} above the $B4$ ground state. The inclusion of the anion polarization changes the lattice energy at the minimum to ~ -835 kJ mol^{-1}, still ~ 55 kJ mol^{-1} above the ground state. As a result, the antilitharge structure is not a viable intermediate *for the model used here*. It is worth stressing, however, that this does not preclude this structure as being an intermediate in other systems, as the relative stability of the antilitharge structure compared to the $B3$ or $B4$ structures is heavily dependent upon the specifics of the ion polarization and, as a result, will vary from system to system. For the highly polarizable cation and anion in AgI, for example, these effects may be such as to bring the antilitharge structure into contention as an intermediate.

TABLE III. Variation of the times for the cell lengths and angles to evolve with barostat parameter (τ_b) and cell size.

Run	τ_b (a.u.)	t_2-t_1 (ps)	t_3-t_2 (ps)
216-1	10000	0.17	0.12
216-2	50000	1.29	0.48
216-3	75000	2.76	0.73
216-4	100000	3.95	1.54
1000-1	10000	0.40	0.21

VI. EFFECT OF BAROSTAT PARAMETERS AND SYSTEM SIZE

Having established a mechanism and a pressure transition range for the $B3\rightarrow B1$ transformation we shall now investigate the effect of parameters of the simulation, such as the system size and the rate at which the pressure is ramped, on the observations.

Figure 8 shows the pressure-volume hysteresis for four runs with the 216-ion system ($3\times3\times3$ unit cells) with barostat parameters τ_b ranging from 10 000 a.u. (used for the run described in detail above) to 10 0000 a.u. The figure also shows the p-V curve for the run using 1000 ions ($5\times5\times5$ unit cells) with barostat parameters of 10 000 a.u. It is clear that both the barostat parameters and the system size have a small, but significant, effect on the pressure range over which the transformation takes place. The increase in the barostat parameter (that is, reducing the rate at which the barostats act to exert the applied pressure) causes the transition to occur both at a higher pressure and over a wider pressure range. The effect of the barostat parameters can be assessed by considering the evolution of the cell lengths and cell angles (as shown in Fig. 6). In order to assess their role we choose to identify three specific times in the phase transition: namely, the time at which the cell lengths begin to distort from cubic to tetragonal (t_1), the time at which the cell angles begin to change (t_2), and the time at which the cell angles reach their final value (t_3) (see Fig. 6). Table III lists the time differences (t_2-t_1) and (t_3-t_2), that is, the time from the beginning to the tetragonal distortion to the change in cell angle and the time for the anion sublattice to rearrange as monitored by the change in cell angle. Both times are seen to increase (essentially linearly) with barostat parameter as would be expected from the equations of motion governing the time evolution of the cell parameters. For a shorter barostat relaxation time the system can act more quickly to bring the system to the required pressure, effectively driving the transition more rapidly. In addition, Fig. 8 shows how the pressure range over which the transition occurs is dependent upon the barostat parameters.

TABLE IV. Variation of the pressure range of transformation and final cell angles with barostat parameter (τ_b) and cell size. The final column lists the number of Σ_3 grain boundaries present in the final structure.

Run size	τ_b (a.u.)	$\theta_{\alpha\beta}$ (rad)			Pressure range (GPa)	Grain boundaries
		xy	xz	yz		
216-1	10 000	1.57	1.91	1.57	12-15	0
216-2	50 000	1.23	1.57	1.57	12-17.5	0
216-3	75 000	1.57	1.57	1.69	12-17.5	2
216-4	100 000	1.57	1.69	1.57	15-21	2
1000-1	10 000	1.57	1.91	1.57	15-21	0

However, the choice of barostat parameters effects more than just the transition pressure. Table IV lists the final cell angles obtained for the five observed $B3 \rightarrow B1$ transitions. For the two runs with barostat parameters of 10 000 a.u. and the one run with a parameter of 50 000 a.u. the final cell angles are $\simeq 110°$ (or, equivalently, 70°), corresponding to an ideal close-packed anion sublattice reoriented with respect to the original $B3$ lattice in the manner described above. However, for both the 75 000 and 100 000 a.u. barostat parameters the final cell angles are around 97°, more acute than the ideal packing arrangement. Figure 12 shows molecular graphics ''snapshots'' of the final ion coordinates for both the slowest and most rapid barostat relaxation times. The upper panel, corresponding to a 10 000 a.u. parameter, is a perfect slab of $B1$ crystal with the $[111]_{B1}$ direction pointing vertically up the page. The lower panel, for a 100 000 a.u. parameter, clearly shows the formation of a pair of mirror-twin Σ_3 grain boundaries (the cell has been doubled to highlight the formation of a boundary at the cell edge).

The formation of the Σ_3 grain boundaries can be readily understood from the considerations of the correlated cation motion discussed previously. The strength of the cation-cation correlations in the $[100]_{B3}$ and $[010]_{B3}$ directions means that idealized layers, in which all the cations have shifted in the same sense, form throughout regardless of the precise details of the simulation procedure. The correlation in the $[001]_B$ direction is much more susceptible to changes in simulation conditions. For short barostat relaxation times these correlations are promoted. Once a single ideal cation layer has formed, the concerted shift in the anion sublattice leads to a significant stress on the simulation cell which acts to promote further cascading of the anion sublattice and, as a result, promotes the correlated motion of the cations in the layers above and below. For slower relaxation times this driving force is greatly reduced and so cation layers form from both motion in the $[100]_{B3}$ and $[\bar{1}00]_{B3}$ directions with subsequent formation of the Σ_3 grain boundaries.

This subtle balance is highlighted by estimating the grain boundary energy from

$$U^{gb} = \frac{U^{gb}_{cell} - U^{crys}_{cell}}{A}, \tag{6.1}$$

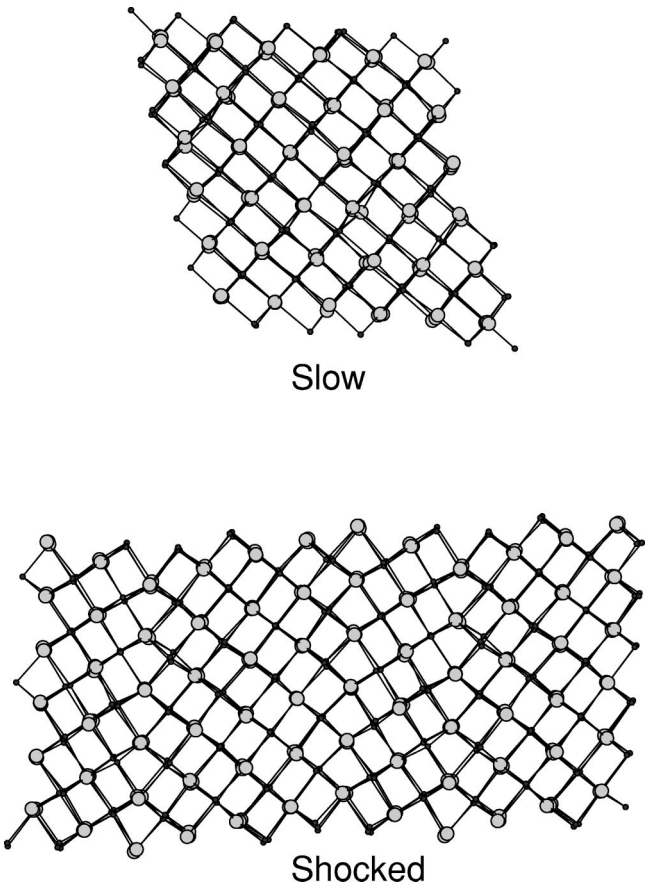

FIG. 12. Molecular graphics snapshots of two final $B1$ structures viewed in the original $B3$ [011] plane. The upper structure is for a relatively slow transformation in which the system pressure is gradually increased, while the lower figure has been obtained by shocking the cell via the application of an instantaneous large pressure. The formation of the low-energy Σ_3 boundaries in the lower figure is clear.

where U^{gb}_{cell} and U^{crys}_{cell} are the energies of the perfect system and that containing a single boundary at the same state point, and A is the boundary surface area. This gives a value of $\simeq 0.1$ Jm^{-2} which is small compared with typical ionic values.[55] Indeed, the Σ_3 boundary is experimentally observed as having the lowest formation energy in systems such as NiO (see Ref. 55 and references therein).

At the other extreme, Σ_3 grain boundaries can also be readily formed by shocking the $B3$ system using a pressure much greater than the actual transition pressure. The number of grain boundaries formed depends essentially upon the ''choice'' of the direction of motion of each cation layer. Once the cations move in a particular direction the massive excess pressure ensures they continue in that direction. As a result, the number of grain boundaries is governed by the *a priori* equivalent choice of direction for each cation layer.

As might be expected from the above discussion, the presence of such strong (and relatively long-ranged) correlations results in significant system size effects. The 1000-ion system, utilizing the same barostat parameters as the run described above in detail, gives a pressure transition at around 15–20 GPa compared with a range of 12–15 GPa for the

108-ion system. The differences in both the pressure range of the transition and the time scale of the transition (as monitored by the times in Table III) reflect the effect of the larger system.

VII. CONCLUSIONS

In this paper two pressure-driven phase transitions have been studied by computer simulation techniques. The two transitions chosen for study (the δ-$ZnCl_2 \rightarrow CdCl_2$ in $ZnCl_2$ and $B3 \rightarrow B1$ in ''MCl'') are simply related in that the starting crystals have cubically close-packed anion lattices with cations in tetrahedral holes.

The transition mechanisms have been shown to be closely related. In both cases a displacive mechanism is observed in which the formed six-coordinate octahedra comprise of the four anions in the original tetrahedral nearest-neighbor cation shell, along with two ions gained from the former next-nearest-neighbor shell. In both cases, highly correlated cation motions are observed during the transformation. The differences between the two mechanisms have been attributed to the layered nature of the $ZnCl_2$ structures which leads to the near loss of cation-cation correlations between layers. The $B3 \rightarrow B1$ mechanism has been found to proceed via an initial distortion to a diatomic β-tin-like structure which was, in turn, shown to be a transition state rather than a full-blown intermediate. The choice of system size and barostat parameters was found to effect the pressure range for transition, although not the mechanism itself.

ACKNOWLEDGMENTS

M.W. thanks the Royal Society for support. The work was supported by EPSRC through Grant No. GR/L/49369 and a studentship for F.H.

APPENDIX

The Ewald reciprocal space charge-charge, charge-dipole, and dipole-dipole contributions to the stress tensor in Eq. (3.5) can be written (in the notation of Nosé and Klein[46]) as follow.

(i) Charge-charge:

$$\Pi_{\alpha\beta}^{qq}=\frac{1}{2\pi V^2}\sum_n{}' \; Q(k_n)\left\{\sum_i q_i\cos(2\pi\mathbf{k}_n\cdot\mathbf{r}_i)\times\sum_j q_j\cos(2\pi\mathbf{k}_n\cdot\mathbf{r}_j)+\sum_i q_i\sin(2\pi\mathbf{k}_n\cdot\mathbf{r}_i)\times\sum_j q_j\sin(2\pi\mathbf{k}_n\cdot\mathbf{r}_j)\right\}$$
$$\times\left\{\delta_{\alpha\beta}-2\frac{(1+\pi^2\eta^2|k_n^2|)}{|k_n|^2}k_{n,\alpha}k_{n,\beta}\right\}, \tag{A1}$$

where $Q(k_n)=e^{-\pi^2|\mathbf{k}_n|^2\eta^2}/|\mathbf{k}_n|^2$ with η the Ewald parameter, typically taken to be $5.0/L$, where L is the shortest simulation cell length.

(ii) Charge-dipole:

$$\Pi_{\alpha\beta}^{q\mu}=\frac{1}{2\pi V^2}\sum_n{}' \; Q(k_n)2\left(\left\{-\sum_i q_i\cos(2\pi\mathbf{k}_n\cdot\mathbf{r}_i)\times\sum_j(2\pi\mathbf{k}_n\cdot\mu_j)\sin(2\pi\mathbf{k}_n\cdot\mathbf{r}_j)+\sum_i q_i\sin(2\pi\mathbf{k}_n\cdot\mathbf{r}_i)\right.\right.$$
$$\times\sum_j(2\pi\mathbf{k}\cdot\mu_j)\cos(2\pi\mathbf{k}_n\cdot\mathbf{r}_j)\Big\}\left\{\delta_{\alpha\beta}-2\frac{(1+\pi^2\eta^2|k_n|^2)}{|k_n|^2}k_{n,\alpha}k_{n,\beta}\right\}+\sum_i 2\pi k_{n,\alpha}\mu_{i,\beta}\cos(2\pi\mathbf{k}_n\cdot\mathbf{r}_i)$$
$$\left.\times\sum_j q_j\sin(2\pi\mathbf{k}_n\cdot\mathbf{r}_j)-\sum_i 2\pi k_{n,\alpha}\mu_{i,\beta}\sin(2\pi\mathbf{k}_n\cdot\mathbf{r}_i)\times\sum_j q_j\cos(2\pi\mathbf{k}_n\cdot\mathbf{r}_j)\right). \tag{A2}$$

(iii) Dipole-dipole:

$$\Pi_{\alpha\beta}^{\mu\mu}=\frac{1}{2\pi V^2}\sum_n{}' \; Q(k_n)\left\{\left(\sum_i(2\pi\mathbf{k}_n\cdot\mu_i)\cos(2\pi\mathbf{k}_n\cdot\mathbf{r}_i)\times\sum_j(2\pi\mathbf{k}_n\cdot\mu_j)\cos(2\pi\mathbf{k}_n\cdot\mathbf{r}_j)+\sum_i(2\pi\mathbf{k}_n\cdot\mu_j)\sin(2\pi\mathbf{k}_n\cdot\mathbf{r}_i)\right.\right.$$
$$\left.\times\sum_j(2\pi\mathbf{k}_n\cdot\mu_j)\sin(2\pi\mathbf{k}_n\cdot\mathbf{r}_j)\right)\left[\delta_{\alpha\beta}-2\left(\frac{1+\pi^2\eta^2|k_n|^2}{|k_n|^2}\right)k_{n,\alpha}k_{n,\beta}\right]+2\sum_i 2\pi k_{n,\alpha}\mu_{i,\beta}\cos(2\pi\mathbf{k}_n\cdot\mathbf{r}_i)$$
$$\left.\times\sum_j(2\pi\mathbf{k}\cdot\boldsymbol{\mu}_j)\cos(2\pi\mathbf{k}_n\cdot\mathbf{r}_j)+2\sum_i 2\pi k_{n,\alpha}\mu_{i,\beta}\sin(2\pi\mathbf{k}_n\cdot\mathbf{r}_i)\times\sum_j(2\pi\mathbf{k}\cdot\mu_j)\sin(2\pi\mathbf{k}_n\cdot\mathbf{r}_j)\right\}. \tag{A3}$$

The remaining real-space contributions to the stress tensor are readily expressed in standard virial form from the real-space forces.

*Present address: University of Pennsylvania, Department of Chemistry, Philadelphia, PA 19104.
[1] R.J. Nelmes and M.I. McMahon, Semicond. Semimet. **54**, 145 (1998).
[2] G.J Ackland, Phys. Status Solidi B **223**, 361 (2001).
[3] J.R. Chelikowsky, Phys. Rev. B **34**, 5295 (1986).
[4] A. Nazzal and A. Qteish, Phys. Rev. B, **53**, 8262 (1996).
[5] N.E. Christensen, D.L. Novikov, R.E. Alonso, and C.O. Rodriguez, Phys. Status Solidi B **211**, 5 (1999).
[6] A. Zunger, K. Kim, and V. Ozalines, Phys. Status Solidi B, **223**, 369 (2001).
[7] H. Sowa, Z. Kristallogr. **215**, 335 (2000).
[8] H. Sowa, Acta Crystallogr., Sect. A: Found. Crystallogr. **57**, 176 (2001).
[9] H. Sowa, Acta Crystallogr., Sect. A: Found. Crystallogr. **56**, 288 (2000).
[10] D.A. Keen and S. Hull, J. Phys.: Condens. Matter **5**, 23 (1993).
[11] S. Hull and D.A. Keen, Phys. Rev. B **59**, 750 (1999).
[12] G.S. Nunes, P.B. Allen, and J.L. Martins, Phys. Rev. B **57**, 5098 (1998).
[13] S. Hull and D.A. Keen, High Press. Res. **14**, 121 (1995).
[14] S. Hull and D.A. Keen, Phys. Rev. B **50**, 5868 (1994).
[15] M. Hofmann, S. Hull, and D.A. Keen, Phys. Rev. B **51**, 12 022 (1995).
[16] S. Hull, D.A. Keen, W. Hayes, and N.J.G. Gardner, J. Phys.: Condens. Matter **10**, 10 941 (1998).
[17] S. Hull and D.A. Keen, J. Phys.: Condens. Matter **8**, 6191 (1996).
[18] S.H. Tolbert and A.P. Alivisatos, J. Chem. Phys. **102**, 4642 (1995); S.H. Tolbert and A.P. Alivisatos, Annu. Rev. Phys. Chem. **46**, 595 (1995).
[19] L.E. Brus, J.A.W. Harkless, and F.H. Stillinger, J. Am. Chem. Soc. **118**, 4834 (1996).
[20] M. Wilson and P.A. Madden, J. Phys.: Condens. Matter **6**, 159 (1994).
[21] P.A. Madden and M. Wilson, Chem. Soc. Rev. **25(5)**, 339 (1996).
[22] S. Scandolo, M. Bernasconi, G.L. Chiarotti, P. Focher, and E. Tosatti, Phys. Rev. Lett. **74**, 4015 (1995); M. Bernasconi, G.L. Chiarotti, P. Focher, S. Scandolo, E. Tosatti, and M. Parrinello, J. Phys. Chem. Solids **56**, 501 (1995).
[23] C.W.F.T. Pistorius, Prog. Solid State Chem. **11**, 1 (1976).
[24] M.I. McMahon and R.J. Nelmes, Phys. Status Solidi B **198**, 389 (1996).
[25] M.J. Moore and J.S. Kasper, J. Chem. Phys. **48**, 2446 (1968).
[26] P.W. Fowler and P.A. Madden, Mol. Phys. **49**, 913 (1983); Phys. Rev. B **29**, 1035 (1984); **31**, 5443 (1985); J. Phys. Chem. **89**, 2581 (1985); Mol. Phys. **86**, 1019 (1990); H.M. Kelly and P.W. Fowler, *ibid.* **80**, 135 (1993); P.W. Fowler and P.A. Madden, Phys. Rev. B **30**, 6131 (1984); P.W. Fowler and N.C. Pyper, Proc. R. Soc. London, Ser. A **398**, 377 (1985); P.W. Fowler, Mol. Simul. **4**, 320 (1990).
[27] P. Jemmer, P.W. Fowler, M. Wilson, and P.A. Madden, J. Chem. Phys. **111**, 2038 (1999).
[28] C. Domene, P.W. Fowler, P.A. Madden, M. Wilson, and R.J. Wheatley, Chem. Phys. Lett. **314**, 158 (1999).
[29] G.D Mahan and K.R. Subbaswamy, *Local Density Theory of Polarizability* (Plenum, London, 1990).
[30] N.C. Pyper, Adv. Solid State Chem. **2**, 223 (1991).
[31] M. Wilson, P.A Madden, N.C. Pyper, and J.H. Harding, J. Chem. Phys. **104**, 8068 (1996).
[32] N.C. Pyper, Proc. R. Soc. London, Ser. A **352**, 89 (1995).
[33] N.C. Pyper, Chem. Phys. Lett. **220**, 70 (1994).
[34] A.J. Rowley, P. Jemmer, M. Wilson, and P.A. Madden, J. Chem. Phys. **108**, 10 209 (1998).
[35] U. Müller, *Inorganic Structural Chemistry* (Wiley, Chichester, 1993).
[36] C.H. Polsky, L.M. Martinez, K. Leinenweber, M.A. VerHelst, C.A. Angell, and G.H. Wolf, Phys. Rev. B **61**, 5934 (2000).
[37] M. Sakai, N. Kuroda, and Y. Nishina, J. Phys. Soc. Jpn. **54**, 4081 (1985).
[38] N.M. Harrison and V.R. Saunders, J. Phys.: Condens. Matter **4**, 3873 (1992); N.M. Harrison, V.R Saunders, E. Aprà, M. Causà, and R. Dovesi J. Phys.: Condens. Matter **4**, L261 (1992).
[39] R.J. Hemley, H.K. Mao, P.M. Bell, and B.O. Mysen, Phys. Rev. Lett. **57**, 747 (1986).
[40] D.J. Durben and G.H. Wolf, Phys. Rev. B **43**, 2355 (1991).
[41] M.C.C. Ribero, M. Wilson, and P.A. Madden, J. Chem. Phys. **109**, 9859 (1998).
[42] M.C.C. Ribero, M. Wilson, and P.A. Madden, J. Chem. Phys. **110**, 4803 (1999).
[43] H.C. Andersen, J. Chem. Phys. **72**, 2384 (1980).
[44] M. Parrinello and A. Rahman, Phys. Rev. Lett. **45**, 1196 (1980).
[45] G.J. Martyna, D.J. Tobias, and M.L. Klein, J. Chem. Phys. **101**, 4177 (1994).
[46] S. Nosé and M.L. Klein, Mol. Phys. **50**, 1055 (1983).
[47] M.J.L. Sangster and M. Dixon, Adv. Phys. **23**, 247 (1976).
[48] O.H. Nielsen and R.M. Martin, Phys. Rev. B **32**, 3780 (1985).
[49] D.C. Wallace, *Thermodynamics of Crystals* (Wiley, New York, 1972).
[50] M. Born and K. Huang, *Dynamical Theory of Crystal Lattices* (Clarendon, Oxford, 1954).
[51] J. Wang, S. Yip, S.R. Phillpot, and D. Wolf, Phys. Rev. Lett. **71**, 4182 (1993).
[52] X. Li and R. Jeanloz, Phys. Rev. B **36**, 474 (1987).
[53] M. Wilson, P.A. Madden, S.A. Peebles, and P.W. Fowler, Mol. Phys. **88**, 1143 (1996).
[54] M. Wilson and P.A. Madden, J. Chem. Soc., Faraday Trans. **106**, 339 (1997).
[55] A.P. Sutton and R.W. Balluffi, Acta Metall. **35**, 2177 (1987).